

1 Revision 2

2 **A modified genetic model for multiple pulsed**
3 **mineralized processes at the giant Qulong porphyry**
4 **Cu-Mo mineralization system**

5 Word Count: 8544 (including text and references)

6
7 Youye Zheng ^{a*}, Xin Chen ^a, Sangjiancuo Luo ^b, Qiong Ci ^c, Le Zhang ^d, Jiangang Wei
8 ^b, Shunbao Gao ^a, Hao Lin ^a

9 ^a *State Key Laboratory of Geological Processes and Mineral Resources and School of*
10 *Earth Resources, China University of Geosciences, Wuhan 430074, China*

11 ^b *Tibet Julong Copper Industry Limited Company, Lhasa, Tibet 850000, China*

12 ^c *No.2 Geological Party, Tibet Autonomous Region Geological and Mineral*
13 *Exploration and Development Bureau, Lhasa 850000, China*

14 ^d *State Key Laboratory of Isotope Geochemistry, Guangzhou Institute of Geochemistry,*
15 *Chinese Academy of Sciences, Guangzhou, China*

16
17 * Corresponding author.

18 *E-mail address:* zhyouye@163.com (Y. Zheng)

19
20 Submission to: American Mineralogist

21 With 8 Figures and 2 supplementary Tables

22

23

ABSTRACT

24 Porphyry copper deposits (PCD) are economically significant sources of Cu and Mo,
25 formed when metal-rich fluids precipitate at shallow levels, exsolving from
26 underlying magmatic reservoirs at depth. However, the origin and evolution of these
27 metal-rich fluids, whether through episodic enrichment from multiple pulses or a
28 single continuous fluid-release event, remain a subject of controversy. To gain deeper
29 insights into these processes, data on cathodoluminescence (CL) imaging, in-situ trace
30 elements, and Sr isotopes of newly discovered scheelite (Sch 1, Sch 2, and Sch 3)
31 found in three generations of vein types within the giant Qulong porphyry Cu-Mo
32 mineralization system are presented. The anhedral Sch 1 occurs in quartz + magnetite
33 + anhydrite + chalcopyrite veins, exhibiting no obvious zoning in the CL image.
34 These scheelite samples show high concentrations of Mo, Nb, Ta, and $^{87}\text{Sr}/^{86}\text{Sr}$ ratios
35 ranging from 0.70688 to 0.71109. Moreover, they demonstrate enriched rare earth
36 elements (REE) and negative Eu anomalies in the chondrite-normalized pattern,
37 indicative of their formation in relatively oxidized metal-rich fluids during the early
38 high-temperature alteration stage. Among the discovered scheelite varieties, the most
39 volumetrically significant is the subhedral Sch2, which occurs in veins composed of
40 quartz + pyrite + chalcopyrite. In its central region (Sch 2a), Cu-rich cores are
41 dispersed, surrounded by an oscillatory Cu-poor mantle and rim (Sch 2b and 2c), as
42 observed in the CL image. When compared to Sch 1, Sch 2 exhibits lower levels of
43 REE, Nb, Ta, Mo, and $^{87}\text{Sr}/^{86}\text{Sr}$ ratios (ranging from 0.70502 to 0.70578), but higher
44 Cu concentration and positive Eu anomalies. The gradual decrease in Cu content from
45 the core to rim in Sch2, along with its rim's intergrowth with sulfide, suggests the
46 precipitation of Cu during the second pulse of fluids. Euhedral Sch 3 is found in
47 relatively moderate-temperature mineral assemblages within quartz + galena+
48 sphalerite + molybdenite veins. It displays an oscillatory pattern with a Mo-rich core
49 (Sch 3a), an extremely Mo-rich mantle (Sch 3b), and a Mo-poor rim (Sch 3c) in the
50 CL image. Sch 3 shows lower REE, Cu, and Pb contents but variable Mo
51 concentrations in different domains, while consistently recording $^{87}\text{Sr}/^{86}\text{Sr}$ ratios

52 ranging from 0.70498 to 0.70542. These characteristics indicate the precipitation
53 process of Mo and Pb during the third pulse of fluid evolution. The observed shift in
54 mineral assemblages, metal contents, and Sr isotopic components from Sch 1 to Sch 3
55 reflects the occurrence of different fluid pulses within a cooling porphyry Cu-Mo
56 mineralization system. Overall, the three generations of scheelite found at the Qulong
57 porphyry Cu-Mo deposit indicate the occurrence of multiple pulsed flows of
58 magmatic fluids, revealing a more complex fluid evolution for PCD than previously
59 recognized. Notably, Sch 1 exhibits relatively high $^{87}\text{Sr}/^{86}\text{Sr}$ ratios, similar to the
60 post-ore mafic porphyries, which are higher compared to Sch 2 and Sch 3, showing
61 $^{87}\text{Sr}/^{86}\text{Sr}$ ratios similar to the pre- and syn-ore host granite and porphyry. This result
62 implies that mafic magma has significantly contributed to the formation of the first
63 pulse of magmatic fluids, whereas syn-ore granitic magma contributed to the ore
64 fluids responsible for forming the veins containing Sch 2 and Sch 3 in the later stage.
65 Therefore, we propose that volatiles from mafic magma, injected into the porphyry
66 metallogenic system, play a crucial role in the formation of PCD. Additionally, for the
67 first time, the presence of Cu-Mo-W metal endowment in the PCD of the Gangdese
68 magmatic belt is identified, providing valuable new insights into the metallogeny of
69 PCD and offering promising opportunities for tungsten exploration in the collision
70 zone.

71 **Keywords:** Scheelite; PCD; Cu-Mo-W mineralization; In-situ Sr isotope;
72 Cathodoluminescence imaging; Recharge of mafic magma; Gangdese
73

74

INTRODUCTION

75

76

77

78

79

80

81

82

83

84

85

86

The formation of porphyry Cu deposits (PCD) through magmatic-hydrothermal processes has been well-established, supported by geologic, geochemical, and isotopic studies ([Seedorff et al., 2005](#); [Sillitoe, 2010](#); [Buret et al., 2017](#)). These studies have revealed that metals are released from magmatic fluids (>600 °C), driven by heat exsolved from deep-seated sub-volcanic intrusions at a paleodepth of 5–10 km. Eventually, these metals precipitate as sulfides of chalcopyrite and molybdenite in the shallow crust at depths of 1-3 km ([Heinrich, 2007](#); [Sillitoe, 2010](#); [Kouzmanov and Pokrovski, 2012](#)). However, despite this understanding, the source, mechanism, and dimensions of fluid evolution remain largely unclear. Specifically, the deciphering of the source and evolution processes of the metal-rich fluids, whether as a series of superimposed processes involving pulsed fluids or a single and continuous fluid-release event, is crucial for comprehending the formation of PCD.

87

88

89

90

91

92

93

94

95

96

97

98

99

100

101

102

Previous studies have established that both single and continuous metal-rich fluid release and precipitation play significant roles in the formation of magmatic-hydrothermal mineralization systems, often resulting in extensive hydrothermal alteration haloes or spatial zoning of high- to low-temperature metallic elements in various ore clusters or deposits ([Sillitoe, 2010](#)). Studies involving fluid inclusions have further revealed that magmatic-hydrothermal mineralization systems, such as PCD, are generally produced by a single fluid evolution process, characterized by a two-phase fluid of brine and low-density vapor. This fluid is either directly exsolved from the silicate melt ([Shinohara, 1994](#)) or, more likely, separated from a single-phase supercritical fluid ([Burnham, 1979](#); [Cline and Bodnar, 1991](#)). On the other hand, high-precision CA-ID-TIMS U-Pb zircon and Re-Os molybdenite dating have documented episodic magmatic-hydrothermal activities in certain areas. This episodic behavior can be attributed to multiple veins and alterations development, overprinting, or the episodic growth of fertile porphyries ([Spencer et al., 2015](#); [Buret et al., 2016](#); [Tapster et al., 2016](#); [Li et al., 2017](#); [Zhao et al., 2021](#)). Recently, oxygen isotope studies on mineralized quartz veins from porphyry-skarn deposits have led to

103 similar conclusions (Li et al., 2018, 2022). However, evaluating the presence of
104 multiple pulses of metal-rich fluids in PCD is challenging. The intense hydrothermal
105 alteration that often occurs can modify or alter primary mineral assemblages.
106 Additionally, evidence of multistage fluids is commonly overprinted or erased by
107 late-stage fluid-rock interactions. Therefore, the main challenge lies in three aspects:
108 (1) identifying multistage-growth domains of hydrothermal minerals that formed
109 throughout magmatic-hydrothermal systems, (2) using these minerals to trace the
110 different stages of exsolved hydrothermal fluids from a vast and long-lived magmatic
111 chamber, and (3) determining how these geochemical changes resulted in different
112 metal mineralization. By clarifying the composition, source, and evolution of
113 multistage fluids that led to metal mineralization, a better understanding of the
114 hydrothermal mineralization processes can be gained, whether they occurred as
115 pulsed events or single and continuous fluid-release events.

116 Scheelite, an important ore mineral, is found across a wide range of pressure,
117 temperature, and chemical (P-T-X) conditions in various types of ore deposits,
118 including skarns, quartz veins, greisen, and orogenic Au deposits (Robert and Brown
119 1986; Ghaderi et al. 1999; Nie et al., 2023). Its distinct textures and zonation patterns
120 can be clearly distinguished using cathodoluminescence (CL) imaging, revealing
121 changes in physical-chemical conditions, dissolution, and replacement during its
122 growth (Wang et al., 2022; Han et al., 2020). Scheelite can form in hydrothermal
123 fluids and incorporate numerous variable valence metals (Fe, Mo, Eu), metal elements
124 (Cu, Pb), and REE (Ghaderi et al. 1999; Brugger et al. 2000; Poulin et al. 2018; Zhao
125 et al. 2018). Due to its complex crystal structure, scheelite can accommodate a large
126 number of major and trace elements, making it valuable in providing information
127 about the nature of the fluids from which it formed (Sciuba et al., 2019). Moreover, its
128 Sr isotopic composition can be used to study fluid origins and fluid-related processes
129 (Darbyshire et al. 1996; Han et al., 2020). Therefore, combining the trace element
130 chemistry of scheelite with its Sr isotope composition can be used to trace the
131 hydrothermal mineralization processes of PCD.

132 In an effort to decipher the source and evolution of ore-forming fluids as either a
133 pulsed phenomenon or a continuous fluid-release event, recently discovered
134 multistage scheelites found in three different classes of mineralization veins within
135 the world-class Qulong porphyry Cu-Mo deposit have been investigated. In this study,
136 cathodoluminescence (CL) images, trace element geochemistry, and Sr isotopic
137 composition of scheelite were utilized as proxies to demonstrate the composition,
138 source, and evolution of the multistage fluids originating from a cooling magma
139 chamber over time. The new findings propose an alternative model for the formation
140 of the Qulong porphyry Cu-Mo mineralization system and provide fresh insights into
141 the metal endowment potential in collision-related PCD.

142 **GEOLOGICAL SETTING**

143 **Geological background**

144 The Lhasa terrane is situated between the Bangong-Nujiang suture zone (BNSZ) to
145 the north and the Indus-Yarlung Zangbo suture zone (IYZSZ) to the south, and it is
146 commonly subdivided into the northern, central, and southern Lhasa terrane ([Fig. 1](#)).
147 These regions are separated by the Shiquan River-Nam Tso melange zone (SNMZ)
148 and the Luobadui-Milashan fault (LMF) from north to south ([Yin and Harrison, 2000](#);
149 [Zhu et al., 2011](#); [Hou et al., 2015a, 2015b](#)). The northern Lhasa subterrane is
150 characterized by juvenile crust containing early Cretaceous medium-K calc-alkaline
151 arc volcanic rocks and granitoids, overlain by Middle Triassic to Cretaceous
152 sedimentary rocks ([Zhu et al., 2013](#); [Hou et al., 2015a](#)). On the other hand, the central
153 Lhasa terrane represents a possible microcontinent, which experienced multiple
154 metamorphic events during the Neoproterozoic ([Guynn et al., 2012](#)). The southern
155 Lhasa terrane within the Gangdese magmatic belt consists of Mesozoic to Cenozoic
156 granitoids and is predominantly composed of juvenile crust with depleted mantle-like
157 Nd-Hf isotopic signatures. This region is covered by the Paleogene Linzizong
158 volcanic succession, along with thin successions of sedimentary rocks ([Mo et al.,](#)

159 2007, 2008; Ji et al., 2009; Zhu et al., 2011, 2013; Ma et al., 2018). The southern
160 Lhasa terrane has undergone complex structural evolution, including late
161 Triassic-Middle Jurassic Neo-Tethys ocean subduction, subsequent continental
162 collision from the early Eocene Indo-Eurasian to the late Oligocene-Miocene, and a
163 post-extension setting (23–12 Ma) along with Miocene N-S rifts (Yin and Harrison,
164 2000; Hou and Cook, 2009; Zhu et al., 2011; Chen et al., 2020; Fan et al., 2023). In
165 this region, the major metallogenic events can be categorized into the
166 Triassic-Jurassic porphyry Cu-Au and the Miocene–Oligocene porphyry-skarn
167 Cu-Mo(-Au) mineralization (Lang et al., 2014; Hou et al., 2015; Chen et al., 2020).
168 The Miocene–Oligocene porphyry-skarn related mineralization is of particular
169 significance and is regarded as one of the most important porphyry-type deposits in
170 China. It encompasses a series of large PCDs, including Jiama, Qulong, Chongjiang,
171 Tinggong, Beimulang, and Zhunuo from east to west (Fig. 1; Hou et al., 2009, 2015a,
172 2015b; Zheng et al., 2004, 2014; Sun et al., 2021; Liu et al., 2022; Wu et al., 2022).

173 **Ore deposit geology**

174 The giant Qulong porphyry Cu-Mo deposit (29°36'–29°40' N, 91°33'–91°37'E)
175 is situated in the eastern part of the Gangdese magmatic belt (Fig. 2) and boasts
176 substantial ore-proven reserves of 2200 Mt Cu @ 0.5% and 500 Mt Mo @ 0.04%
177 (Zheng et al., 2004; Li et al., 2017). The deposit's formation involved the intrusion of
178 pre-ore Rongmucuola intrusions and ore-related monzogranitic porphyries into the
179 Mesozoic Yeba Formation, which comprises a series of rhyolite, dacite-rhyolite
180 porphyry, and volcanic-sedimentary rocks (Fig. 2; Zheng et al., 2004). The pre-ore
181 Rongmucuola intrusions consist of biotite monzogranite (17.4 ± 0.6 Ma) in the center,
182 surrounded by granodiorite (17.9 ± 0.5 Ma) (Zhao et al., 2016). Meanwhile, the
183 syn-ore porphyries mainly comprise monzogranitic porphyries (16.9 ± 0.5 Ma) in the
184 central area (Yang et al., 2009; Zhao et al., 2016). As for the post-ore lithology, the
185 dioritic porphyries (15.7 ± 0.2 Ma) form dikes intruding into the rocks located above
186 (Yang et al., 2015). The alteration zones exhibit a typical concentric alteration pattern,

187 featuring potassic alteration overprinted by late phyllic and argillic alteration to
188 varying degrees, extending to the outer propylitic zone (Yang et al., 2009). Potassic
189 alteration assemblages, characterized by secondary K-feldspar, magnetite, anhydrite,
190 and biotite, dominate in the deep sections of the monzogranitic porphyry and
191 granodiorite porphyry. An intruding hydrothermal breccia pipe displays potassic
192 alteration, with an abundance of biotite and magnetite, subsequently overprinted by
193 late phyllic alteration (Fig. 2; Yang et al., 2009; Li et al., 2017; Yu et al., 2022). The
194 phyllic alteration zone is located in the monzogranitic porphyries and the peripheral
195 biotite monzogranite, surrounding and superimposing the potassic alteration zone
196 (Zheng et al., 2004). The Cu-Mo orebodies are primarily hosted in the biotite
197 monzogranite, monzogranite porphyry, and central hydrothermal breccia pipe (Fig. 2;
198 Zheng et al., 2004; Yang et al., 2009). The deposits consist of multiple stock veins,
199 ranging from early-stage veinlets associated with biotite + quartz + anhydrite +
200 magnetite + scheelite (Fig. 3a-b), quartz + magnetite + pyrite + chalcopyrite veins
201 (Fig. 3c), and K-feldspar + quartz veins to late-stage pyrite + chalcopyrite + scheelite
202 veins (Fig. 3d-h) and quartz + galena + Ag-rich tetrahedrite + sphalerite +
203 molybdenite + scheelite veins (Fig. 3i-k) with Cu-Fe-Mo sulfide minerals. Copper
204 mineralization is predominantly linked to potassic and phyllic alteration (Yang et al.,
205 2009; Li et al., 2017). The orebodies exhibit stockwork and disseminated
206 mineralization, primarily composed of chalcopyrite, molybdenite, pyrite, and scheelite
207 (Fig. 3; Zheng et al., 2004; Yang et al., 2009).

208 SAMPLING AND METHODOLOGY

209 Samples

210 Representative samples containing scheelite were selected from drilled holes
211 (ZK307, ZK303, ZK407, and ZK1412) at the Qulong deposit (Fig. 2). The
212 distribution of scheelite in these drilled holes was examined using an ultraviolet
213 fluorescent lamp. Approximately 25 scheelite-bearing samples were then prepared as
214 40-50 μm thick thin sections for observation under reflected and transmitted light

215 microscopy to characterize their paragenetic relationships. Scheelite is primarily
216 found in magnetite-bearing veins (sample ZK303-915), chalcopyrite-bearing veins
217 (sample ZK407-689), and galena-sphalerite-molybdenite-bearing veins (ZK307-974).
218 As a result, scheelite samples extracted from these three types of veins were subjected
219 to scanning electron microscope (SEM) cathodoluminescence, major and trace
220 elements, and Sr isotope analysis.

221 **SEM cathodoluminescence of scheelite**

222 In order to decipher the distinct textures and zonation patterns, SEM CL images of
223 scheelite were recorded using an Analytical Scanning Electron Microscope coupled
224 with a GATAN MINICL system. The applied acceleration voltage and current were
225 approximately 10-13 kV and ca. 80-85 nA, respectively.

226 **Major and trace element composition of scheelite**

227 The major and trace element concentrations of scheelite were determined at the
228 Wuhan SampleSolution Analytical Technology Co., Ltd., Wuhan, China. Laser
229 sampling was performed using a GeolasPro laser ablation system, which consists of a
230 COMPexPro 102 ArF excimer laser (wavelength of 193 nm and maximum energy of
231 200 mJ) along with a MicroLas optical system. To acquire ion-signal intensities, an
232 Agilent 7700e ICP-MS instrument was employed. During the ablation process, helium
233 was used as the carrier gas. Each spot analysis incorporated approximately 30s of
234 background acquisition, followed by 40s of data acquisition from the sample. A spot
235 size of 32 μm was used together with a repetition rate of 8 Hz, and an energy density
236 of 5.5 $\text{J}\cdot\text{cm}^{-2}$. After every 8-10 sample analyses, several analyses of external reference
237 materials were conducted. For quality control (QC) purposes, NIST SRM 610 was
238 utilized as the reference material to correct the instrumental time-dependent
239 sensitivity drift. External calibration was carried out using multiple external standards,
240 namely NIST 610, BHVO-2G, BCR-2G, BIR-1G, and GSE-1G. The preferred
241 concentrations for the reference glasses were obtained from the GeoReM database
242 (<http://georem.mpch-mainz.gwdg.de/>). To process the data, off-line selection and
243 integration of background and analyte signals, time drift correction, and quantitative

244 calibration were performed using ICPMSDataCal 10.9 (Liu et al., 2008). The
245 time-resolved signals for each analyzed spot were thoroughly reviewed. The
246 analytical precisions for most measured elements were better than 8%, and the results
247 were found to agree with their reference values within $\pm 10\%$. The major and trace
248 element data for minerals determined using LA-ICP-MS are listed in **Appendix Table**
249 **A1**.

250 **In situ LA–MC–ICP–MS Sr isotopes of scheelite**

251 The Sr isotope ratios of scheelite were analyzed using a Neptune Plus
252 MC-ICP-MS (Thermo-Scientific) coupled with a RESOLUTION M-50 193 nm laser
253 ablation system at the State Key Laboratory of Isotope Geochemistry, Guangzhou
254 Institute of Geochemistry, Chinese Academy of Sciences. For each single laser spot
255 ablation, the spot diameter ranged from 112 to 180 μm , depending on the Sr signal
256 intensity. The pulse frequency was set at 6 Hz, while the laser fluence remained
257 constant at approximately $4 \text{ J}\cdot\text{cm}^{-2}$. To correct for ^{87}Rb , the measured natural
258 $^{85}\text{Rb}/^{87}\text{Rb}$ value of 2.593 (Catanzaro et al., 1966) was used. The mass bias of $^{87}\text{Sr}/^{86}\text{Sr}$
259 was normalized to $^{86}\text{Sr}/^{88}\text{Sr} = 0.1194$ with an exponential law. For in situ Sr isotope
260 analysis of scheelite, a natural sample of plagioclase, PZHPI, was used as the
261 (unknown) sample. The detailed data reduction procedure was previously reported by
262 Zhang et al. (2018).

263 **RESULTS**

264 **Scheelite distribution and classification**

265 Based on vein type, mineral assemblage, and CL images, three generations of
266 scheelite (Sch 1, Sch 2, and Sch 3) associated with mineralization can be
267 distinguished (Fig. 3 and 4). Sch 1 is mainly distributed in the quartz + magnetite +
268 anhydrite + chalcopyrite veins as disseminations (Fig. 4a-b). It is characterized by
269 weak oscillation zoning in the CL image (Fig. 4c), with no obvious compositional
270 zoning. Sch 2 is the most commonly found stage associated with Cu ore and occurs as
271 quartz \pm chalcopyrite \pm pyrite veinlets (Fig. 4d). According to the CL image, Sch 2

272 displays homogeneity and dispersal in the core (Sch 2a), along with oscillatory zoning
273 in the bright mantle (Sch 2b) and dark rim (Sch 2c) (Fig. 4e-f). Sch 3 occurs as veins
274 intergrown with quartz, galena, sphalerite, and molybdenite (Fig. 4g-h) and can be
275 categorized into three sub-types based on the CL image (Fig. 4i). Sch 3a exhibits a
276 homogeneous texture and bright color in the core, while Sch 3b displays a grey color
277 without zoning in the mantle. Sch 3c is brighter than Sch 3b and displays
278 well-developed oscillatory zoning texture (Fig. 4i).

279 Major and trace element geochemistry

280 A total of 60 major and trace elements were analyzed using LA-ICP-MS for
281 three generations of scheelite at the Qulong deposit (Appendix Table A1). These
282 scheelite grains exhibit similar major element compositions, with WO_3 ranging from
283 74.82% to 81.06% and CaO ranging from 15.60% to 19.55%. However, they display
284 variable abundances of trace elements such as Sr, Y, Zr, Nb, Ta, Mo, U, Pb, and rare
285 earth elements (REEs). The positive correlation between Na and REEs (Fig. 5a) in
286 scheelite suggests that the REEs are likely incorporated into the scheelite structure
287 through a Na substitution mechanism (Ghaderi et al. 1999).

288 Among the three generations of scheelite, Sch 1 shows the highest REE content,
289 ranging from 1244 to 2664 ppm (Fig. 6a). It is high in Y (345-1179 ppm), Sr (342-519
290 ppm), Pb (17.0-27.3 ppm), Nb (3.70-74.4 ppm), Ta (0.07-2.46), Th (5.37-14.1), and
291 Mo (2328-3824 ppm) (Fig. 5b; Appendix Table A1). Sch 1 exhibits flat REE
292 distribution patterns with a negative Eu anomaly ($\text{Eu}/\text{Eu}^*=0.65-0.94$) (Fig. 5b and
293 6a).

294 Sch 2 displays relatively low REE concentrations, ranging from 76.7 to 1789
295 ppm, compared to Sch 1 (Fig. 6b). It shows variable abundances of U (0-403 ppm),
296 Pb (4.84-196 ppm), Nb (1.63-9.45 ppm), Ta (0.02-0.09 ppm), Mo (1.91-336 ppm), Sr
297 (326-959 ppm), Cu (0-16914 ppm), FeO (0-1.42 wt%) (Fig. 5b; Appendix Table A1).
298 It exhibits a MREE-enriched pattern, with strong positive chondrite-normalized Eu
299 anomalies (Fig. 6b). Notably, significant differences in REE content exist among
300 different domains of Sch 2, with the lowest concentration in the mantle (Sch 2b) and

301 the highest in the rim (Sch 2c) (Fig. 6b). The Eu anomalies of Sch 2 demonstrate a
302 negative correlation with Mo contents (Fig. 5b). In comparison, Sch 2a stands out
303 with its high Cu and Fe content when compared to Sch 2b and Sch 2c, and there is a
304 positive correlation between Fe and Cu contents (Fig. 5c).

305 Sch 3 grains were analyzed and found to exhibit mainly positive Eu anomalies
306 (ranging from 0.75 to 6.92) and the lowest total REE contents (ranging from 13.5 to
307 610 ppm) among all the samples analyzed (Fig. 6c). They display low concentrations
308 of U (0-4.41 ppm), Pb (0.66-9.71 ppm), and Cu (0-0.51 ppm), while Mo (0.68-6724
309 ppm) and Sr (195-1110 ppm) contents vary (Fig. 5b; Appendix Table A1). Based on
310 the difference in Mo content, Sch 3 can be divided into three types: Mo-rich Sch 3a
311 core (78.2-397 ppm), extremely Mo-rich Sch 3b mantle (1052-6724 ppm), and
312 Mo-poor Sch 3c rim (0.67-207 ppm) (Fig. 5d). Sch 3a and Sch 3b have relatively low
313 REE contents compared to Sch 3c (Fig. 5c). Additionally, the Eu anomalies of Sch 3
314 show a positive correlation with Mo contents (Fig. 5b).

315 **In situ Sr isotopes of scheelite**

316 The in situ Sr isotopes of three generations of scheelite are presented in Appendix
317 Table A2 and Fig. 7. The $^{87}\text{Sr}/^{86}\text{Sr}$ ratios of anhedral Sch 1 found in the quartz +
318 magnetite + anhydrite + chalcopyrite veins exhibit a wide variation, ranging from
319 0.70688 to 0.71109. In contrast, Sch 2 shows a lower $^{87}\text{Sr}/^{86}\text{Sr}$ ratio (ranging from
320 0.70502 to 0.70578) compared to Sch 1, and these ratios do not vary along the profiles
321 from core to rim within individual scheelite grains. The $^{87}\text{Sr}/^{86}\text{Sr}$ ratios of Sch 3
322 demonstrate little variation and are similar to Sch 2, ranging from 0.70498 to 0.70542.

323

DISCUSSION

324 **Evidence of multistage pulses of fluids**

325 Scheelite CL images, trace-element, and Sr isotope analyses of three generations
326 of mineralization veins (quartz + magnetite + anhydrite + chalcopyrite veins, quartz +
327 pyrite + chalcopyrite veins, and quartz + galena + sphalerite + molybdenite veins) not
328 only provide direct evidence for scheelite formation related to different mineralization

329 stages but also yield valuable information about the source and evolution of ore fluids.
330 The presence of three generations of scheelite in these veins, along with hydrothermal
331 magnetite, chalcopyrite, and molybdenite, strongly suggests their derivation from
332 hydrothermal fluids. Consequently, the cross-cutting nature of these three generations
333 of mineralization veins, displaying poly-cyclic growth scheelite zoning, indicates the
334 crystallization of these veins may be a result of multistage pulsed fluids, recording at
335 least three stages of fluid activities.

336 Anhedra Sch 1 occurs in quartz + magnetite + anhydrite + chalcopyrite veins,
337 displaying no zoning in the CL image (Fig. 4a-c). It exhibits high concentrations of
338 Mo, Nb, Ta, and an enriched pattern of REEs in comparison to chondrites along with
339 negative Eu anomalies (Fig. 5b and 6a). These veins, characterized by early
340 magnetite-bearing veinlets, exhibit varied alteration halos containing albite,
341 K-feldspar, biotite, and anhydrite, with features typical of potassic alteration stage
342 (Fig. 3a-c and 4a-c). Studies of fluid inclusions by Li et al. (2017) show that the early
343 fluids in the potassic alteration stage from the Qulong porphyry system are indicative
344 of high temperatures (~425 °C). These features suggest that they may represent
345 high-temperature fluids exsolved from an upper-crustal magma chamber during the
346 early stages (Richards, 2003; Cooke et al., 2005). The Mo-rich scheelite found in the
347 early veins of the Qulong deposit is intergrown with anhydrite and magnetite (Fig.
348 3a-c and 4a-c), indicating its formation in an oxidized hydrothermal system. Such
349 conditions are conducive to the enrichment and migration of Cu-Mo and other metal
350 elements. This observation is further supported by the presence of a negative Eu
351 anomaly and high Mo contents in Sch 1 (Fig. 5b). The incorporation of Mo (Mo⁶⁺)
352 into scheelite by substituting for W⁶⁺ is facilitated in an oxidized setting (Ghaderi et al.
353 1999; Elbaz-Poulichet et al. 2005; Zhao et al. 2018), making Mo a redox-sensitive
354 element. Additionally, a negative Eu anomaly is typically associated with relatively
355 oxidizing conditions, indicating an enrichment of Eu³⁺ compared to Eu²⁺, while a
356 positive Eu anomaly suggests more reducing conditions (Ghaderi et al. 1999; Brugger
357 et al. 2000; Poulin et al. 2018; Zhao et al. 2018). These findings collectively indicate

358 that Sch 1 likely represents the early-stage pulse of relatively oxidized metal-rich
359 fluids during the high-temperature alteration stage.

360 Subhedral Sch 2 is found in quartz + pyrite + chalcopyrite veins (Fig. 3d-h and
361 4d), which are widely distributed and partially intersect with the early
362 magnetite-bearing veins. The presence of large amounts of chalcopyrite within these
363 quartz-pyrite veins and their associated phyllic alteration haloes suggests that the
364 ore-forming hydrothermal fluids were enriched with reducing S^{2-} and Cu. Li et al.
365 (2017) determined trapping temperatures of 340 and 280 °C in the phyllic alteration
366 stage using liquid–vapor two-phase fluid inclusions, indicating that the subhedral Sch
367 2 formed in moderate-temperature aqueous fluids. Furthermore, the clear negative
368 linear correlation between positive Eu anomalies and low Mo concentration (Fig. 5b)
369 points to the presence of relatively reduced metal-rich fluids during the mineralization
370 process (Ghaderi et al. 1999; Brugger et al. 2000; Elbaz-Poulichet et al. 2005). The
371 CL image reveals conspicuous growth zoning in Sch 2 (Fig. 4e-f), which has
372 remained unaltered by subsequent hydrothermal fluids, making it capable of
373 preserving primary features and the physical-chemical conditions of its formation
374 (Han et al., 2020). Sch 2 exhibits a dispersed Cu-rich core (Sch 2a) and an oscillatory
375 Cu-poor mantle and rim (Sch 2b and 2c) in the CL image (Fig. 4c). The decrease in
376 Cu concentration from Sch 2a to Sch 2b and 2c, along with its rim's intergrowth with
377 sulfide, indicates the precipitation of Cu in a moderate-temperature fluid environment.
378 Consequently, Sch 2 displays lower REE, Nb, Ta, Mo, and $^{87}\text{Sr}/^{86}\text{Sr}$ ratios (ranging
379 from 0.70498 to 0.70542) (Fig. 7), but higher Cu concentration and positive Eu
380 anomalies compared to Sch 1. These characteristics suggest that this stage represents
381 Cu-rich ore fluid pulses responsible for Cu ore formation under middle-temperature
382 conditions.

383 Euhedral Sch 3 is found in mineral assemblages characterized by relatively low
384 temperatures, specifically in quartz + galena + Ag-rich tetrahedrite + sphalerite +
385 molybdenite veins (Fig. 3i-k). Ag-rich tetrahedrite is a common middle- and
386 low-temperature mineral in hydrothermal deposits (Gallego and Akasaka, 2010). Thus,

387 the mineral assemblage of Sch 3 with Ag-rich tetrahedrite, galena and sphalerite,
388 indicates the formation of Sch 3 under middle- to low-temperature conditions. In the
389 CL image (Fig. 4i), Sch 3 displays an oscillatory Mo-rich core (Sch 3a), an extremely
390 Mo-rich mantle (Sch 3b), and a Mo-poor rim (Sch 3c) (Fig. 5d). This arrangement
391 provides insights into the precipitation process of Mo and Pb during fluid evolution.
392 Despite variations in different domains, Sch 3 consistently demonstrates lower levels
393 of REEs, Cu, and Pb, along with variable Mo content. The recorded $^{87}\text{Sr}/^{86}\text{Sr}$ ratios
394 (ranging from 0.70502 to 0.70578) (Fig. 7) remain constant, reflecting the fluid
395 evolution. Notably, a significant positive linear correlation between Eu anomalies and
396 Mo contents (Fig. 5b) suggests that Mo enrichment might be influenced by the Mo
397 content in the fluid rather than the oxygen fugacity of hydrothermal fluids.
398 Consequently, the third generation of fluids is interpreted as representing a Mo-rich
399 fluid pulse originating from the cooling magma chamber.

400 **The source and evolution of pulsed fluids**

401 Based on the preceding discussion, scheelite from three generations of vein types
402 exhibits intricate growth zoning patterns. This suggests that these scheelite samples
403 can serve as indicators of the primary physicochemical conditions during their growth.
404 Notably, $^{87}\text{Rb}/^{86}\text{Sr}$ ratios in scheelite are typically quite low, ranging from 0 to 0.17.
405 As a result, the measured $^{87}\text{Sr}/^{86}\text{Sr}$ ratios can directly reflect the initial Sr isotope
406 composition of the fluid from which scheelite crystallized (Chugaev et al., 2010). The
407 high-temperature fluid exsolution would not alter the Sr-Nd isotope signatures in
408 magmatic systems (Xu et al., 2015; Cao et al., 2021). Therefore, Sr-Nd isotope ratios
409 of hydrothermal scheelite can be used to constrain the source of hydrothermal fluids
410 and their parent magma. Previous studies have established a close connection between
411 the Qulong porphyry Cu-Mo mineralization and the syn-ore monzonitic porphyries
412 (Zheng et al., 2004; Yang et al., 2009; Zhao et al., 2016; Li et al., 2017). However, the
413 newly identified $^{87}\text{Sr}/^{86}\text{Sr}$ values (ranging from 0.70688 to 0.71109) of Sch 1 are
414 higher than those of the pre- and syn-ore host granite and porphyry ($^{87}\text{Sr}/^{86}\text{Sr}$);
415 0.704847–0.705237; Fig. 7; Yang et al., 2015). These values align more closely with

416 those from post-ore mafic porphyries ($(^{87}\text{Sr}/^{86}\text{Sr})_i$: 0.707004–0.707198; Yang et al.,
417 2015) and postcollisional ultrapotassic rocks from southern Tibet (Yang et al., 2016).
418 This similarity implies that volatile components from more radiogenic mafic and
419 ultrapotassic magma might have significantly contributed to the formation of
420 Mo-W-rich magmatic fluids. Sch 2 and Sch 3, characterized by chalcopyrite and
421 molybdenite mineralization, exhibit a comparable Sr isotope composition. This
422 composition is akin to that of the pre- and syn-ore host granite and porphyry. Such
423 similarity suggests that the primary metal-enriched fluids likely originated from either
424 the syn-ore granitic magma or from an interaction between fluids emanating from the
425 radiogenic mafic magma and exsolved hydrothermal fluids from the monzonitic
426 porphyries. Consequently, the variations in isotopic ratios observed in scheelite across
427 the three generations of vein types could potentially signify the involvement of
428 multiple fluid and metal sources in the formation of the collision-related PCD.

429 The formation of three generations of scheelite and veins offers a record of the
430 progressive evolution of exsolved fluids within a cooling porphyry metallogenic
431 system. Initial fluids from the porphyry system are enriched in metals and sulfur,
432 representing an oxidizing nature. The subsequent two fluid generations, which might
433 represent evolved fluids originating from the magmatic chamber, exhibit relatively
434 different oxidation states, creating favorable conditions for the late stage precipitation
435 of Cu and Mo enrichment. The sequential exsolution of Cu- and Mo-rich fluids at
436 distinct time intervals from the magmatic chamber could potentially result in their
437 spatial separation. Consequently, the pulsed evolution of fluids and the gradual
438 cooling process significantly contribute to the precipitation of Cu, Mo, and W.

439 **A modified genetic model for the world-class Qulong porphyry deposit**

440 As discussed earlier, the following modified model is presented to elucidate the
441 formation of the W-bearing world-class Qulong porphyry deposit through the
442 hydrothermal evolution involving multiple stages of scheelite formation (Fig. 8). The
443 initial stage is linked to pre-ore magmatic processes, resulting in the development of
444 the Rongmucuola granite host (Fig. 8a; Zhao et al., 2016; Li et al., 2017). This

445 granitic magma exhibited relatively low volatile content, which did not give rise to
446 significant Cu mineralization or alteration. Subsequently, it is presumed that the felsic
447 magma reservoir underwent enrichment through the exsolution of volatiles from the
448 underlying mafic magma into the overlying felsic mush (Fig. 8b). Supporting
449 evidence comes from Sch-1 found in the quartz + magnetite + anhydrite + pyrite veins,
450 exhibiting $^{87}\text{Sr}/^{86}\text{Sr}$ ratios comparable to those of high-Mg dioritic porphyries and
451 postcollisional ultrapotassic rocks in southern Tibet (Yang et al., 2015, 2016). Yang et
452 al. (2015) and Sun et al. (2018) proposed that mantle-derived high-Mg dioritic and
453 postcollisional ultrapotassic magmas would increase water content through
454 differentiation, influencing the Cu ore-forming fertility of porphyry intrusions.
455 Additionally, previous research has demonstrated that mafic magmas derived from
456 metasomatized mantle contain elevated volatile components and metals, including Cu
457 and S (Hattori and Keith, 2001; Halter et al., 2005; Seedorff et al., 2005), which were
458 repeatedly injected into the felsic magma chamber (Hollings et al., 2011; Cao et al.,
459 2018). This injection likely introduced a substantial amount of ore-forming elements
460 (Hattori, 1993; Hattori and Keith, 2001; Cao et al., 2018), as supported by examples
461 such as Bingham and Black Mountain (Hattori and Keith, 2001; Zhang and Audétat,
462 2017; Cao et al., 2018, 2019), reinforcing the validity of this model. Hence,
463 high-temperature fluid exsolution from the mafic melt is likely to have higher
464 concentrations of volatiles such as water and S compared to the fluids exsolved from
465 the overlying felsic mush, leading to the localized formation of early stage
466 independent quartz + magnetite + anhydrite + chalcopryrite veins. These
467 high-temperature fluids might further migrate, blend with lower-temperature fluids
468 originating from the overlying felsic mush, and potentially engage with host rocks.
469 This could trigger subsequent fluid pulses, marked by the precipitation of Sch-2 and
470 Sch-3 during the process of fluid evolution and cooling. Volatiles released from the
471 mafic melt can also induce alterations in the morphology and structure of minerals
472 (Blundy et al., 2015). For instance, zircons exhibiting dark CL zoning in the
473 Alumbrera Au-rich PCD signify their origin from the mafic melt infusion into the

474 magma chamber. The subsequent release of volatile matter during growth can lead to
475 uneven crystallization of zircons (Buret et al., 2016). Additionally, the influence of
476 high-temperature volatiles, coupled with the mafic melt input, can result in the
477 development of disequilibrium phenocryst zoning, embayed quartz crystals, and
478 cumulate clots (Wark et al., 2007; Cao et al., 2018, 2021). In light of this, both
479 petrographic and chemical evidence from scheelite suggests that the influx of fluids
480 through a mafic recharge event introduced substantial quantities of volatiles into the
481 porphyry system. This process assumes vital importance in the formation of
482 collision-related PCD.

483 **IMPLICATIONS**

484 The synthesis of currently available data encompassing petrography, CL analyses,
485 in-situ trace element, and Sr isotope data of scheelite derived from three generations
486 of vein types at the Qulong PCD reveals a record of temporal and spatial overlap of
487 multiple hydrothermal events. The distinctive characteristics of these three
488 generations of scheelite, including varied metal compositions, REE patterns, and
489 $^{87}\text{Sr}/^{86}\text{Sr}$ values, suggest that the fluid influx was marked by superimposed, episodic
490 hydrothermal pulses. This contrasts with the notion of a singular, continuous release
491 of metal-rich fluids. The first generations of scheelite, characterized by high
492 concentrations of Mo, Nb, Ta, elevated $^{87}\text{Sr}/^{86}\text{Sr}$ values, and high REEs along with
493 negative Eu anomalies in the chondrite-normalized pattern, indicates its formation
494 within relatively oxidized metal-rich fluids during the early high-temperature
495 alteration stage. The second and third generations of scheelite, found within distinct
496 temperature mineral assemblages, display varying concentrations of Cu and Mo. This
497 discrepancy suggests the occurrence of separate Cu-rich and Mo-rich ore fluid pulses,
498 potentially leading to local decoupling of Cu-Mo mineralization. Therefore, the rapid
499 and episodic release of such fluids offers an explanation for the presence of multiple
500 mutually intersecting vein types and the widespread overlay of extensive multipulsed
501 alteration and mineralization phenomena. These fluids could have undergone

502 migration, intermixing with other fluid types, and interaction with host rocks,
503 consequently triggering metal precipitation throughout the course of fluid evolution
504 and cooling. The duration and timing intervals of fluid pulses directly influence the
505 efficiency of fluid exsolution and metal precipitation. Rapid and multi-stage fluid
506 pulsing is particularly conducive to the expansion of mineral deposit scales. Moreover,
507 Sch-1 exhibits relatively high $^{87}\text{Sr}/^{86}\text{Sr}$ ratios, akin to those of the post-ore mafic
508 porphyries. This contrasts with Sch-2 and Sch-3, which present similar $^{87}\text{Sr}/^{86}\text{Sr}$ ratios
509 to the pre-ore and syn-ore host granite and porphyry. These findings suggest a
510 significant contribution of mafic magma to the initiation of the first pulse of magmatic
511 fluids, whereas syn-ore granitic magma plays a role in supplying ore fluids for the
512 formation of Sch-2- and Sch-3-bearing veins in the subsequent stages. Therefore, our
513 proposition suggests that volatiles originating from mafic rocks, injected into the
514 porphyry metallogenic system, assume a pivotal role in shaping PCD formation. The
515 recent findings demonstrate that scheelite, displaying discernible internal textures
516 across various vein generations, offers essential insights into the genesis and
517 evolutionary trajectory of ore fluids. This represents a significant stride forward in
518 comprehending the intricate development of multi-stage pulsed ore fluids derived
519 from an upper-crustal magma chamber within the context of porphyry Cu-Mo
520 mineralization systems.

521 Furthermore, the co-occurrence of scheelite with quartz + pyrite+ chalcopyrite
522 veins and quartz + galena + sphalerite + molybdenite veins displays a discernible
523 spatial progression, becoming more pronounced at greater depths within the vein
524 system, culminating from 700 to 900 m at the Qulong deposit. This finding bears
525 significant implications for future exploration endeavors. The recognition of
526 Cu-Mo-W mineralization within the Qulong PCD of the Gangdese magmatic belt
527 offers valuable novel insights, shedding light on the potential for identifying
528 complementary metal endowments of W-Cu-Mo and extending the metallogenic
529 scope of PCD within collision zones. Given the Qulong PCD's status as a prototypical
530 representative of the Gangdese magmatic belt, the search for tungsten (W) potential

531 could emerge as a promising new avenue for exploration, positioning it as an
532 innovative target for collision-related PCD investigations.

533 **Acknowledgments**

534 We express our sincere gratitude to the Editor-in-Chief Prof. Dr. Don Baker and
535 Associate Editor Prof. Dr. Thomas Mueller of American Mineralogist for their
536 efficient handling and valuable constructive comments. Our heartfelt thanks extend to
537 Dr. Zheng Liu for providing invaluable assistance in data interpretation, as well as to
538 the other members of our team for their dedicated support during fieldwork. We also
539 acknowledge the Fundamental Research Fund for the National Natural Science
540 Foundation of China (No.42372092; No. U22A20572) and the Postdoctoral Science
541 Foundation of China (BX20220277, 2022M722938).

542

543 **References**

- 544 Blundy, J., Mavrogenes, J., Tattitch, B., Sparks, S., and Gilmer, A. (2015). Generation
545 of porphyry copper deposits by gas–brine reaction in volcanic arcs. *Nature*
546 *Geoscience*, 8(3), 235-240.
- 547 Burnham, C. W. (1979). Magmas and hydrothermal fluids. *Geochemistry of*
548 *hydrothermal ore deposits*, 71-136.
- 549 Brugger, J., Bettioli, A. A., Costa, S., Lahaye, Y., Bateman, R., Lambert, D. D., and
550 Jamieson, D. N. (2000). Mapping REE distribution in scheelite using
551 luminescence. *Mineralogical Magazine*, 64(5), 891-903.
- 552 Buret, Y., von Quadt, A., Heinrich, C., Selby, D., Wälle, M., and Peytcheva, I. (2016).
553 From a long-lived upper-crustal magma chamber to rapid porphyry copper
554 emplacement: Reading the geochemistry of zircon crystals at Bajo de la
555 Alumbrera (NW Argentina). *Earth and Planetary Science Letters*, 450, 120-131.
- 556 Buret, Y., Wotzlaw, J. F., Roozen, S., Guillong, M., von Quadt, A., and Heinrich, C. A.
557 (2017). Zircon petrochronological evidence for a plutonic-volcanic connection in

- 558 porphyry copper deposits. *Geology*, 45(7), 623-626.
- 559 Cao, M., Hollings, P., Cooke, D. R., Evans, N. J., McInnes, B. I., Qin, K., and Baker,
560 M. (2018). Physicochemical processes in the magma chamber under the Black
561 Mountain porphyry Cu-Au deposit, Philippines: Insights from mineral chemistry
562 and implications for mineralization. *Economic Geology*, 113(1), 63-82.
- 563 Cao, M., Evans, N. J., Hollings, P., Cooke, D. R., McInnes, B. I., and Qin, K. (2021).
564 Apatite texture, composition, and O-Sr-Nd isotope signatures record magmatic
565 and hydrothermal fluid characteristics at the Black Mountain porphyry deposit,
566 Philippines. *Economic Geology*, 116(5), 1189-1207.
- 567 Cao, K., Yang, Z. M., White, N. C., and Hou, Z. Q. (2022). Generation of the giant
568 porphyry Cu-Au deposit by repeated recharge of mafic magmas at Pulang in
569 eastern Tibet. *Economic Geology*, 117(1), 57-90.
- 570 Cao, K., Yang, Z. M., Mavrogenes, J., White, N. C., Xu, J. F., Li, Y., and Li, W. K.
571 (2019). Geology and genesis of the giant Pulang porphyry Cu-Au district,
572 Yunnan, Southwest China. *Economic Geology*, 114(2), 275-301.
- 573 Catanzaro, E.J., Murphy, T.J., Garner, E.L., and Shields, W.R. (1966) Absolute
574 isotopic abundance ratio and atomic weight of terrestrial rubidium. *Journal of*
575 *Research of the National Bureau of Standards*, 73, 511–516.
- 576 Chen, X., Zheng, Y., Gao, S., Wu, S., Jiang, X., Jiang, J., and Lin, C. (2020a). Ages
577 and petrogenesis of the late Triassic andesitic rocks at the Luerma porphyry Cu
578 deposit, western Gangdese, and implications for regional metallogeny.
579 *Gondwana Research*, 85, 103-123.
- 580 Chen, H., Cui, H., Zhong, R., Xie, Y., Yu, C., Li, Z., and Ling, Y. (2020b). Solubility
581 of Na₂SO₄ in silica-saturated solutions: Implications for REE mineralization.
582 *American Mineralogist*, 105(11), 1686-1694.
- 583 Chugaev, A. V., Chernyshov, I. V., Gamyagin, G. N., Bortnikov, N. S., and Baranova,
584 A. N. (2010). Rb-Sr isotopic systematic of hydrothermal minerals, age, and
585 matter sources of the Nezhdaninskoe gold deposit (Yakutia). In *Doklady Earth*
586 *Sciences* (Vol. 434, No. 2, p. 1337). Springer Nature BV.

- 587 Cline, J. S., and Bodnar, R. J. (1991). Can economic porphyry copper mineralization
588 be generated by a typical calc-alkaline melt? *Journal of Geophysical Research:*
589 *Solid Earth*, 96, 8113-8126.
- 590 Cui, H., Zhong, R., Xie, Y., Wang, X., and Chen, H. (2021). Melt–fluid and fluid–
591 fluid immiscibility in a Na₂SO₄–SiO₂–H₂O system and implications for the
592 formation of rare earth deposits. *Acta Geologica Sinica-English Edition*, 95(5),
593 1604-1610.
- 594 Darbyshire, D. P. F., Pitfield, P. E. J., and Campbell, S. D. G. (1996). Late Archean
595 and Early Proterozoic gold-tungsten mineralization in the Zimbabwe Archean
596 craton: Rb-Sr and Sm-Nd isotope constraints. *Geology*, 24(1), 19-22.
- 597 Elbaz-Poulichet, F., Seidel, J. L., Jézéquel, D., Metzger, E., Prévot, F., Simonucci, C.,
598 and Radakovitch, O. (2005). Sedimentary record of redox-sensitive elements (U,
599 Mn, Mo) in a transitory anoxic basin (the Thau lagoon, France). *Marine*
600 *Chemistry*, 95(3-4), 271-281.
- 601 Fan, J. J., Zhang, X. Z., Ma, L., Wang, Q., Jiang, Z. Q., Xia, X. P., Wei, G., Wang, Z.,
602 Zhou, J., Li, Q., Liu, X., Huang, T., Zhang, M., Liu, J. H. (2023). Formation of
603 Eocene– Miocene felsic magmatic rocks along NS– trending
604 Yardo-Kongbugang mountain ranges in the eastern Himalaya: New insights into
605 surface uplift and the initiation of EW extension in southern Tibet. *Geological*
606 *Society of America Bulletin*. <https://doi.org/10.1130/B36617.1>
- 607 Gallego Hernández, A. N., Akasaka, M. (2010). Ag-rich Tetrahedrite in the El
608 Zancudo Deposit, Colombia: Occurrence, Chemical Compositions and Genetic
609 Temperatures. *Resource geology*, 60(3), 218-233.
- 610 Ghaderi, M., Palin, J. M., Campbell, I. H., and Sylvester, P. J. (1999). Rare earth
611 element systematics in scheelite from hydrothermal gold deposits in the
612 Kalgoorlie-Norseman region, Western Australia. *Economic Geology*, 94(3),
613 423-437.
- 614 Guynn, J., Kapp, P., Gehrels, G. E., and Ding, L. (2012). U–Pb geochronology of
615 basement rocks in central Tibet and paleogeographic implications. *Journal of*

- 616 Asian Earth Sciences, 43(1), 23-50.
- 617 Hattori, K. H., and Keith, J. D. (2001). Contribution of mafic melt to porphyry copper
618 mineralization: evidence from Mount Pinatubo, Philippines, and Bingham
619 Canyon, Utah, USA. *Mineralium Deposita*, 36, 799-806.
- 620 Halter, W. E., Heinrich, C. A., and Pettke, T. (2005). Magma evolution and the
621 formation of porphyry Cu–Au ore fluids: evidence from silicate and sulfide melt
622 inclusions. *Mineralium Deposita*, 39, 845-863.
- 623 Hattori, K. (1993). High-sulfur magma, a product of fluid discharge from underlying
624 mafic magma: evidence from Mount Pinatubo, Philippines. *Geology*, 21(12),
625 1083-1086.
- 626 Han, J., Chen, H., Hong, W., Hollings, P., Chu, G., Zhang, L., and Sun, S. (2020).
627 Texture and geochemistry of multi-stage hydrothermal scheelite in the
628 Tongshankou porphyry-skarn Cu-Mo (-W) deposit, eastern China: Implications
629 for ore-forming process and fluid metasomatism. *American Mineralogist*, 105(6),
630 945-954.
- 631 Heinrich, C. A. (2007). Fluid-fluid interactions in magmatic-hydrothermal ore
632 formation. *Reviews in Mineralogy and Geochemistry*, 65(1), 363-387.
- 633 Hollings, P., Cooke, D. R., Waters, P. J., and Cousens, B. (2011). Igneous
634 geochemistry of mineralized rocks of the Baguio district, Philippines:
635 Implications for tectonic evolution and the genesis of porphyry-style
636 mineralization. *Economic Geology*, 106(8), 1317-1333.
- 637 Hou, Z., Duan, L., Lu, Y., Zheng, Y., Zhu, D., Yang, Z., and McCuaig, T. C. (2015a).
638 Lithospheric architecture of the Lhasa terrane and its control on ore deposits in
639 the Himalayan-Tibetan orogen. *Economic Geology*, 110(6), 1541-1575.
- 640 Hou, Z., Yang, Z., Lu, Y., Kemp, A., Zheng, Y., Li, Q., Tang, J., Yang, Z., and Duan, L.
641 (2015b). A genetic linkage between subduction- and collision-related porphyry
642 Cu deposits in continental collision zones. *Geology*, 43, 247-250.
- 643 Hou, Z., and Cook, N. J. (2009). Metallogensis of the Tibetan collisional orogen: A
644 review and introduction to the special issue. *Ore Geology Reviews*, 36(1-3),

- 645 2-24.
- 646 Hu, Y. B., Liu, J. Q., Ling, M. X., Ding, W., Liu, Y., Zartman, R. E., and Sun, W. D.
647 (2015). The formation of Qulong adakites and their relationship with porphyry
648 copper deposit: geochemical constraints. *Lithos*, 220, 60-80.
- 649 Ji, W. Q., Wu, F. Y., Chung, S. L., Li, J. X., and Liu, C. Z. (2009). Zircon U–Pb
650 geochronology and Hf isotopic constraints on petrogenesis of the Gangdese
651 batholith, southern Tibet. *Chemical Geology*, 262(3-4), 229-245.
- 652 Lang, X., Tang, J., Li, Z., Huang, Y., Ding, F., Yang, H., Zhou, Y. (2014). U–Pb and
653 Re–Os geochronological evidence for the Jurassic porphyry metallogenic event
654 of the Xiongcu district in the Gangdese porphyry copper belt, southern Tibet,
655 PRC. *Journal of Asian Earth Sciences*, 79, 608-622.
- 656 Li, Y., Selby, D., Condon, D., and Tapster, S. (2017). Cyclic magmatic-hydrothermal
657 evolution in porphyry systems: High-precision U–Pb and Re–Os geochronology
658 constraints on the Tibetan Qulong porphyry Cu–Mo deposit. *Economic Geology*,
659 112(6), 1419-1440.
- 660 Li, Y., Li, X. H., Selby, D., and Li, J. W. (2018). Pulsed magmatic fluid release for the
661 formation of porphyry deposits: Tracing fluid evolution in absolute time from the
662 Tibetan Qulong Cu–Mo deposit. *Geology*, 46(1), 7-10.
- 663 Li, Y., Allen, M. B., and Li, X. H. (2022). Millennial pulses of ore formation and an
664 extra-high Tibetan Plateau. *Geology*, 50(6), 665-669.
- 665 Liu, Y., Hu, Z., Gao, S., Günther, D., Xu, J., Gao, C. and Chen, H. (2008) In situ
666 analysis of major and trace elements of anhydrous minerals by LA-ICP-MS
667 without applying an internal standard. *Chemical Geology* 257, 34-43.
- 668 Liu, P., Wu, S., Zheng, Y., Wang, X., Kang, Y., Yan, J., and Chen, L. (2022). Geology
669 and factors controlling the formation of the newly discovered Beimulang
670 porphyry Cu deposit in the western Gangdese, southern Tibet. *Ore Geology
671 Reviews*, 144, 104823.
- 672 Ma, X., Meert, J. G., Xu, Z., and Yi, Z. (2018). Late Triassic intra-oceanic arc system
673 within Neotethys: Evidence from cumulate appinite in the Gangdese belt,

- 674 southern Tibet. *Lithosphere*, 10(4), 545-565.
- 675 Nie, L., Wang, F., White, N. C., Zhang, D., Yan, C., and Wang, X. (2023). Scheelite
676 trace element compositions: A robust new tool for mineral exploration. *Ore
677 Geology Reviews*, 105338.
- 678 Kouzmanov, K., and Pokrovski, G.S., 2012. Hydrothermal controls on metal
679 distribution in porphyry Cu (-Mo-Au) systems. Society of Economic Geologists,
680 Special Publication, 16, 573–618.
- 681 Poulin, R. S., Kontak, D. J., McDonald, A., and McClenaghan, M. B. (2018).
682 Assessing scheelite as an ore-deposit discriminator using its trace-element and
683 REE chemistry. *The Canadian Mineralogist*, 56(3), 265-302.
- 684 Richards, J. P. (2003). Tectono-magmatic precursors for porphyry Cu-(Mo-Au)
685 deposit formation. *Economic geology*, 98(8), 1515-1533.
- 686 Robert, F., and Brown, A. C. (1986). Archean gold-bearing quartz veins at the Sigma
687 Mine, Abitibi greenstone belt, Quebec; Part II, Vein paragenesis and
688 hydrothermal alteration. *Economic Geology*, 81(3), 593-616.
- 689 Seedorff, E., Dilles, J.H., Proffett, J.M., Jr., Einaudi, M.T., Zurcher, L., Stavast,
690 W.J.A., Johnson, D.A. and Barton, M.D. (2005). Porphyry Deposits:
691 Characteristics and Origin of Hypogene Features. *Economic Geology*, 251–298
692 (100th Anniversary Volume 1905–2005).
- 693 Sillitoe, R.H. (2010) Porphyry Copper Systems. *Economic Geology*, 105, 3-41.
- 694 Sciuba, M., Beaudoin, G., Grzela, D., and Makvandi, S. (2020). Trace element
695 composition of scheelite in orogenic gold deposits. *Mineralium Deposita*, 55,
696 1149-1172.
- 697 Shinohara, H. (1994). Exsolution of immiscible vapor and liquid phases from a
698 crystallizing silicate melt: Implications for chlorine and metal transport.
699 *Geochimica et Cosmochimica Acta*, 58(23), 5215-5221.
- 700 Spencer, E. T., Wilkinson, J. J., Creaser, R. A., and Seguel, J. (2015). The distribution
701 and timing of molybdenite mineralization at the El Teniente Cu-Mo porphyry
702 deposit, Chile. *Economic Geology*, 110(2), 387-421.

- 703 Sun, X., Hollings, P., and Lu, Y. J. (2021). Geology and origin of the Zhunuo
704 porphyry copper deposit, Gangdese belt, southern Tibet. *Mineralium Deposita*,
705 56, 457-480.
- 706 Sun, S. S., and McDonough, W. F. (1989). Chemical and isotopic systematics of
707 oceanic basalts: implications for mantle composition and processes. *Geological*
708 *Society, London, Special Publications*, 42(1), 313-345.
- 709 Tapster, S., Condon, D. J., Naden, J., Noble, S. R., Petterson, M. G., Roberts, N. M.
710 W., and Smith, D. J. (2016). Rapid thermal rejuvenation of high-crystallinity
711 magma linked to porphyry copper deposit formation; evidence from the Koloula
712 Porphyry Prospect, Solomon Islands. *Earth and Planetary Science Letters*, 442,
713 206-217.
- 714 Wark, D. A., Hildreth, W., Spear, F. S., Cherniak, D. J., and Watson, E. B. (2007).
715 Pre-eruption recharge of the Bishop magma system. *Geology*, 35(3), 235-238.
- 716 Wang, M., Zhao, R., Shang, X., Wei, K., Liu, K., and An, W. (2022). REE and
717 cathodoluminescence features of scheelites from the Tongshankou Cu–Mo
718 deposit in Eastern China. *Ore Geology Reviews*, 147, 104998.
- 719 Wu, S., Zheng, Y., Xu, B., Jiang, G., Yi, J., Liu, X., and Li, L. (2022). Heterogeneous
720 mantle associated with asthenosphere and Indian slab metasomatism: Constraints
721 on fertilization of porphyry Cu mineralization in Tibetan orogen. *Ore Geology*
722 *Reviews*, 140, 104601.
- 723 Xu, W.G., Fan, H.R., Hu, F.F., Santosh, M., Yang, K.F., and Lan, T.G. (2015). In situ
724 chemical and Sr-Nd-O isotopic compositions of apatite from the Tongshi
725 intrusive complex in the southern part of the North China craton: Implications
726 for petrogenesis and metallogeny. *Journal of Asian Earth Sciences*, 105, 208–
727 222.
- 728 Yang, Z., Hou, Z., White, N.C., Chang, Z., Li, Z. and Song, Y. (2009). Geology of the
729 post-collisional porphyry copper–molybdenum deposit at Qulong, Tibet. *Ore*
730 *Geology Reviews* 36, 133-159.
- 731 Yang, Z., Lu, Y.-j., Hou, Z. and Chang, Z. (2015) High-Mg Diorite from Qulong in

- 732 Southern Tibet: Implications for the Genesis of Adakite-like Intrusions and
733 Associated Porphyry Cu Deposits in Collisional Orogens. *Journal of Petrology*
734 56, 227-254.
- 735 Yin, A. and Harrison, T.M. (2000) Geologic Evolution of the Himalayan-Tibetan
736 Orogen. *Annual Review of Earth and Planetary Sciences*, 28, 211-280.
- 737 Yu, K., Li, G., Zhao, J., Evans, N. J., Li, J., Jiang, G., Guo, H., 2022. Biotite
738 composition as a tracer of fluid evolution and mineralization center: A case study
739 at the Qulong porphyry Cu-Mo deposit, Tibet. *Mineralium Deposita*, 57(6),
740 1047-1069.
- 741 Zheng, Y., Xue, Y., Cheng, L., Fan, Z. and Gao, S. (2004) Finding, Characteristic and
742 significances of Qulong Superlarge porphyry Copper (Molybdenum) Deposit,
743 Tibet. *Earth Science* 29. 1, 103-108 (in Chinese with English abstract).
- 744 Zheng, Y., Sun, X., Gao, S., Zhao, Z., Zhang, G., Wu, S., You, Z., and Li, J. (2014).
745 Multiple mineralization events at the Jiru porphyry copper deposit, southern
746 Tibet: Implications for Eocene and Miocene magma sources and resource
747 potential. *Journal of Asian Earth Sciences*, 79, 842-857.
- 748 Zhang, L., Ren, Z.Y., Wu, Y.D., and Li, N. (2018) Sr isotope measurement of basaltic
749 glasses by LA-MC-ICP-MS based on a linear relationship between analytical
750 bias and Rb/Sr ratios. *Rapid Communications in Mass Spectrometry*, 32, 105–
751 112.
- 752 Zhang, D., and Audétat, A. (2017). What caused the formation of the giant Bingham
753 Canyon porphyry Cu-Mo-Au deposit? Insights from melt inclusions and
754 magmatic sulfides. *Economic Geology*, 112(2), 221-244.
- 755 Zhao, Q., Zhai, D., Mathur, R., Liu, J., Selby, D., and Williams-Jones, A. E. (2021).
756 The giant Chalukou porphyry Mo deposit, northeast China: The product of a
757 short-lived, high flux mineralizing event. *Economic Geology*, 116(5), 1209-1225.
- 758 Zhao, J., Qin, K., Xiao, B., McInnes, B., Li, G., Evans, N., and Li, J. (2016). Thermal
759 history of the giant Qulong Cu–Mo deposit, Gangdese metallogenic belt, Tibet:
760 constraints on magmatic–hydrothermal evolution and exhumation. *Gondwana*

- 761 Research, 36, 390-409.
- 762 Zhao, W. W., Zhou, M. F., Williams-Jones, A. E., and Zhao, Z. (2018). Constraints on
763 the uptake of REE by scheelite in the Baoshan tungsten skarn deposit, South
764 China. *Chemical Geology*, 477, 123-136.
- 765 Zhu, D. C., Zhao, Z. D., Niu, Y., Dilek, Y., and Mo, X. X. (2011). Lhasa terrane in
766 southern Tibet came from Australia. *Geology*, 39(8), 727-730.
- 767 Zhu, D.C., Zhao, Z.D., Niu, Y., Dilek, Y., Hou, Z.Q. and Mo, X.X. (2013). The origin
768 and pre-Cenozoic evolution of the Tibetan Plateau. *Gondwana Research*, 23,
769 1429–1454.

770 **FIGURE AND TABLE CAPTION**

771

772 **Fig. 1** Distribution of tectonic framework and Miocene porphyry copper deposits of
773 the Lhasa terrane (modified after [Hou et al., 2015a](#)). Abbreviations: BNSZ =
774 Bangong-Nujiang Suture Zone, GLZCF = Gar–Lunggar–Zhari Nam Tso–Comai
775 Fault, LMF = Luobadui-Milashan Fault, SNMZ = Shiquanhe-Nam Tso Melange
776 Zone, IYZSZ = Indus-Yarlung Zangbo Suture Zone, SLT = southern Lhasa
777 terrane, CLT = central Lhasa terrane, NLT = northern Lhasa terrane.

778 **Fig. 2** (a) Deposit geology map of the Qulong porphyry Cu-Mo deposit ([modified](#)
779 [from Yang et al., 2009 and Zhao et al., 2016](#)). (b) simplified geological condition
780 of drill hole refers to ZK-numbers and depth.

781 **Fig. 3** Hand specimen photographs of veins and alteration in the monzogranite and
782 monzonitic porphyry at the Qulong deposit. (a-c) Hydrothermal breccias with
783 early veins with mineral assemblages of quartz + magnetite + anhydrite +
784 chalcopryrite; (d-h) Monzogranite with quartz + scheelite + pyrite + chalcopryrite

785 veins and intensive phyllic alteration; (i-k) Late stage veins with mineral
786 assemblages of quartz + galena+ sphalerite + molybdenite veins intruded into the
787 monzogranite Abbreviations: Sch = Scheelite, Mag = Magnetite, Ccp =
788 Chalcopyrite, Anh = Anhydrite, Qz = Quartz, Py = Pyrite, Sp = sphalerite, Mol =
789 Molybdenite, Gn = galena. Mineral abbreviation according to Whitney and
790 Evans (2010).

791 **Fig. 4** Representative photomicrographs of three generations of scheelite at the
792 Qulong deposit. (a-b) Anhedral Sch 1 occurs in a quartz + anhydrite + magnetite
793 + chalcopyrite vein; (c) Anhedral Sch 1 with dispersive zoning in CL image; (d)
794 Subhedral Sch 2 intergrowth with quartz + pyrite + chalcopyrite + rutile veins;
795 (e-f) Sch 2 with dispersed Cu-rich core (Sch 2a) and oscillatory mantle (Sch 2b)
796 and rim (Sch 2c) in CL image; (g-h) Euhedral Sch 3 intergrowth with quartz,
797 galena, sphalerite, Ag-rich tetrahedrite, and molybdenite in the veinlet; (i) Sch 3
798 exhibits an oscillatory zone with bright core (Sch 3a), dark mantle (Sch 3b), and
799 oscillatory bright rim (Sch 3c) in the CL image. Abbreviations: Sch = Scheelite,
800 Mag = Magnetite, Ccp = Chalcopyrite, Anh = Anhydrite, Qz = Quartz, Py =
801 Pyrite, Rt = Rutile, Sp = sphalerite, Mol = Molybdenite, Gn = galena; Te =
802 tetrahedrite.

803 **Fig. 5** Selected trace elemental variation of three generations of scheelite (a) Eu/Eu*
804 vs. Mo, (b) REE+Y vs. Na, (c) Fe vs Cu, (d) Mo vs. WO₃.

805 **Fig. 6** Chondrite-normalized REE patterns of three generations of scheelite from the
806 Qulong deposit. Data are normalized by values of chondrite (Sun and

807 [McDonough 1989](#)).

808 **Fig. 7** In situ Sr isotopes for three generations of scheelite compared with whole-rock
809 Sr isotopes of the Rongmucuola pluton, monzogranitic porphyries, and High-Mg
810 diorite porphyry in the Qulong deposit. The data of Rongmucuola pluton,
811 monzogranitic porphyries, High-Mg diorite porphyry, and postcollisional
812 ultrapotassic rocks from southern Tibet are from ([Yang et al., 2015, 2016](#); [Hu et](#)
813 [al., 2015](#))

814 **Fig. 8** Schematic illustration showing the genetic model of the Qulong porphyry
815 Cu-Mo deposit. (a) Crystallization of pre-ore monzogranite and granodiorite with
816 weak mineralization and alteration; (b) Metal-rich volatiles from mafic rocks
817 injected in the depth into the porphyry metallogenic system and provide metals
818 and sulphurous gases for formation of syn-ore monzogranitic porphyries, sulfide,
819 and scheelite.

820 **Appendix Table A1.** LA-ICP-MS major and trace elemental data of three generations
821 of scheelite at the Qulong deposit.

822 **Appendix Table A2.** LA-MC-ICP-MS Sr isotopes of three generations of scheelite at
823 the Qulong deposit.

824

825

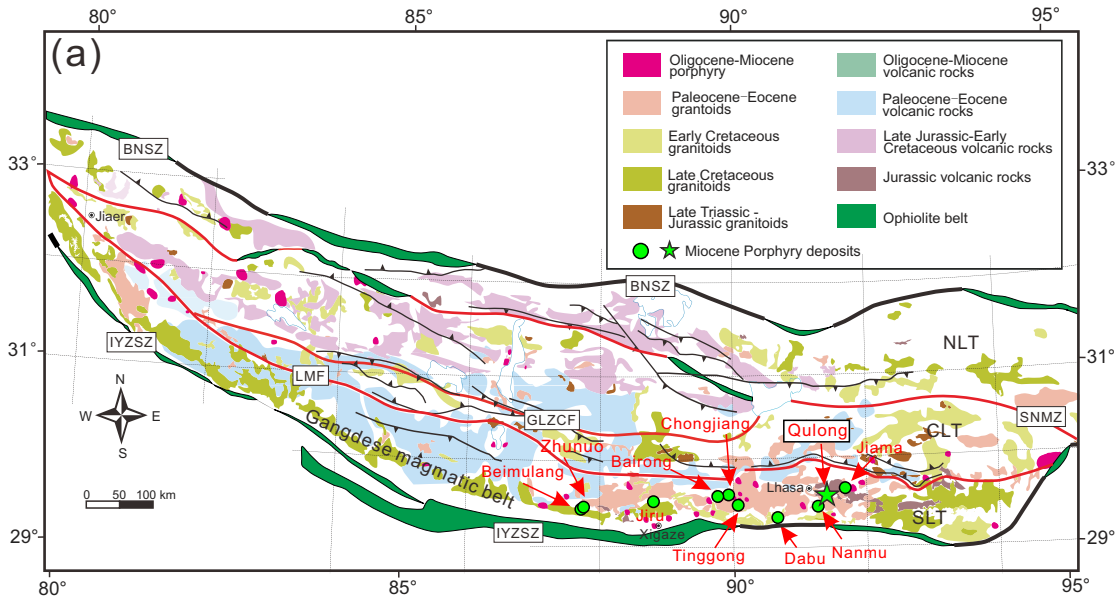


Figure 1

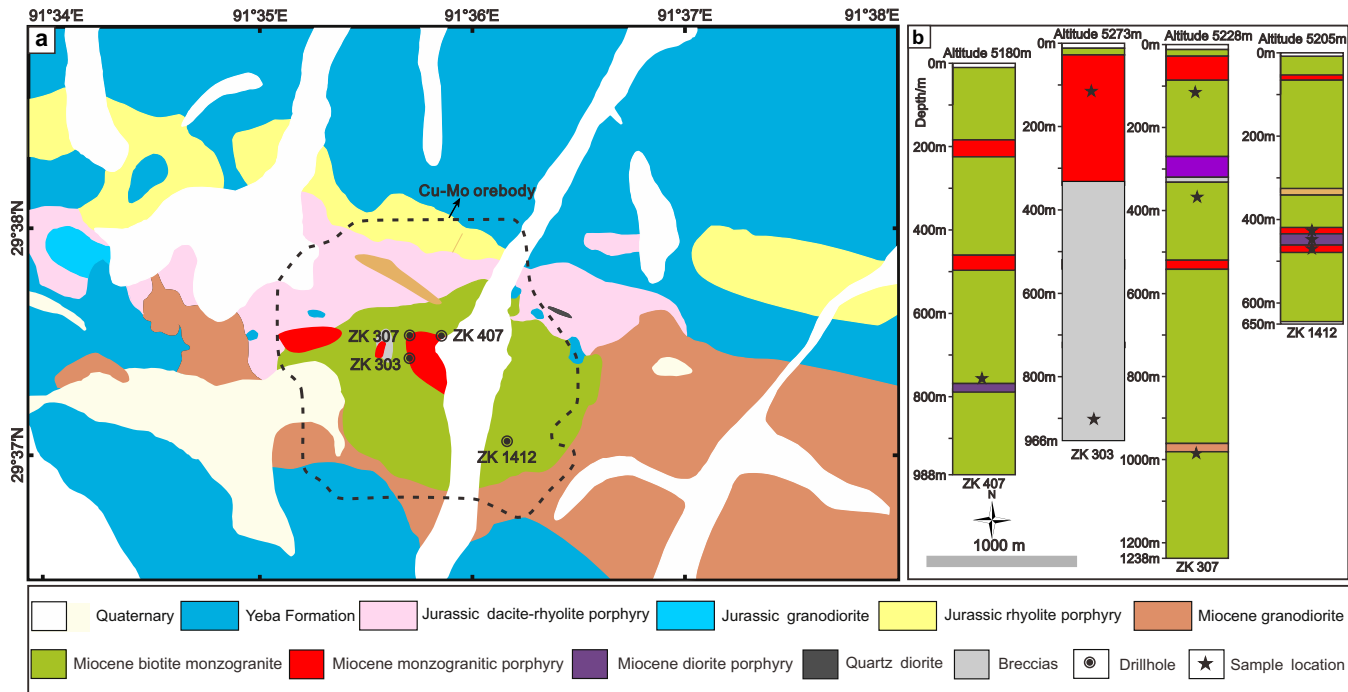


Figure 2

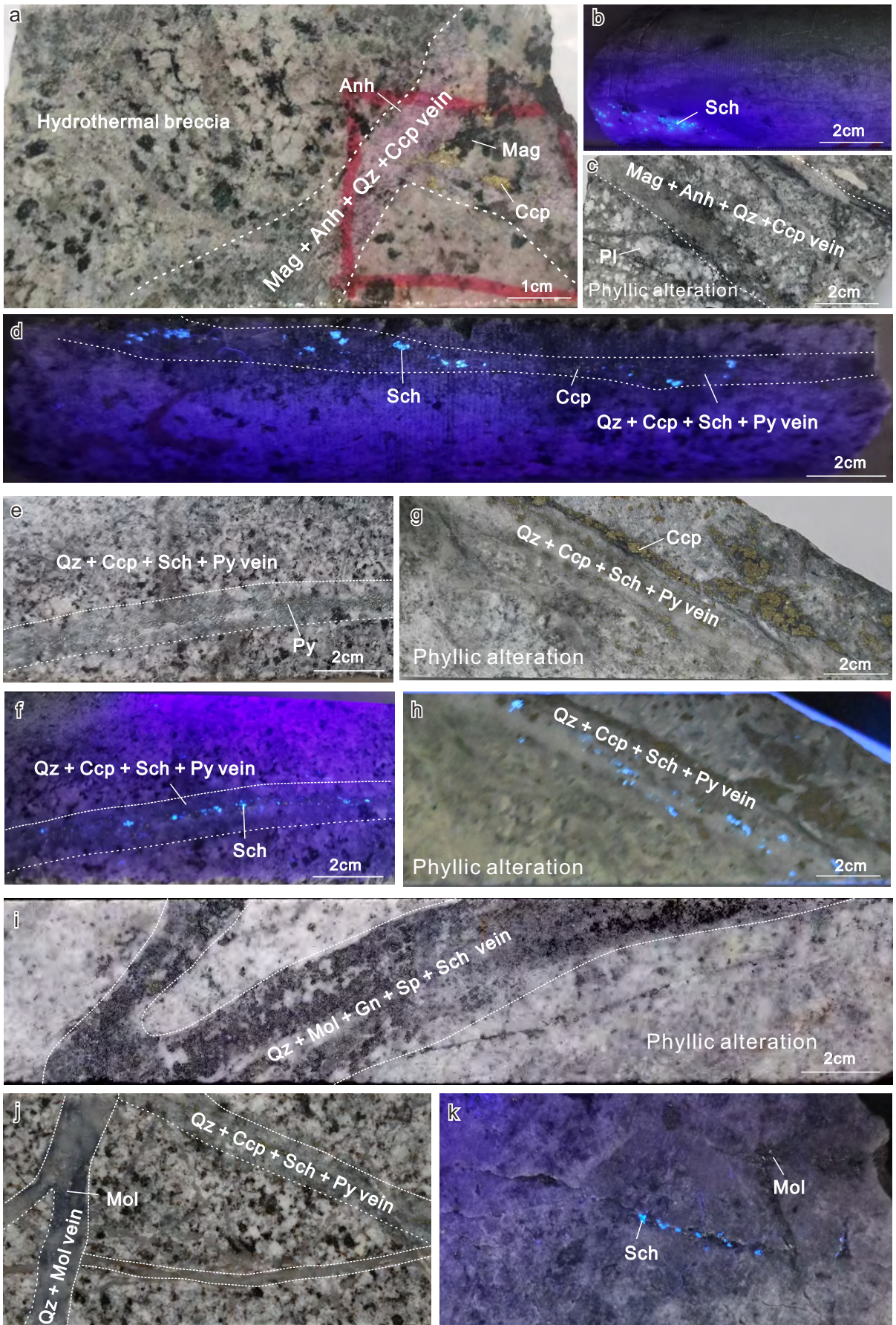


Figure 3

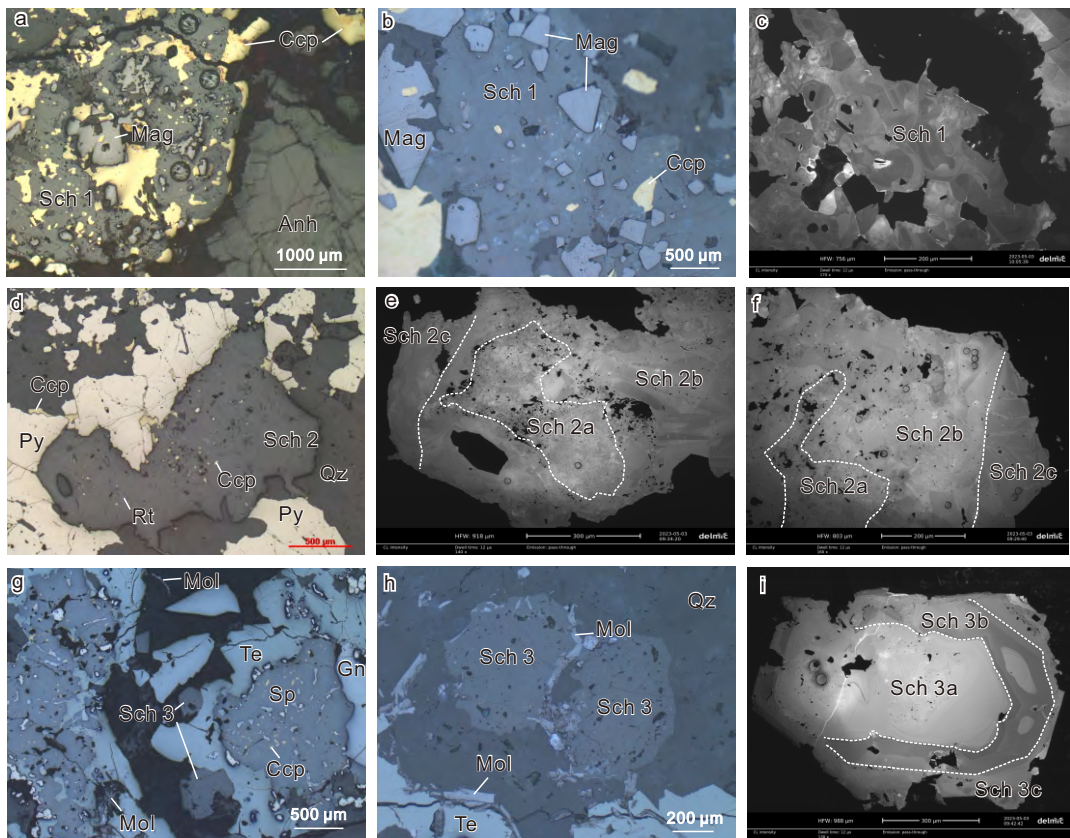


Figure 4

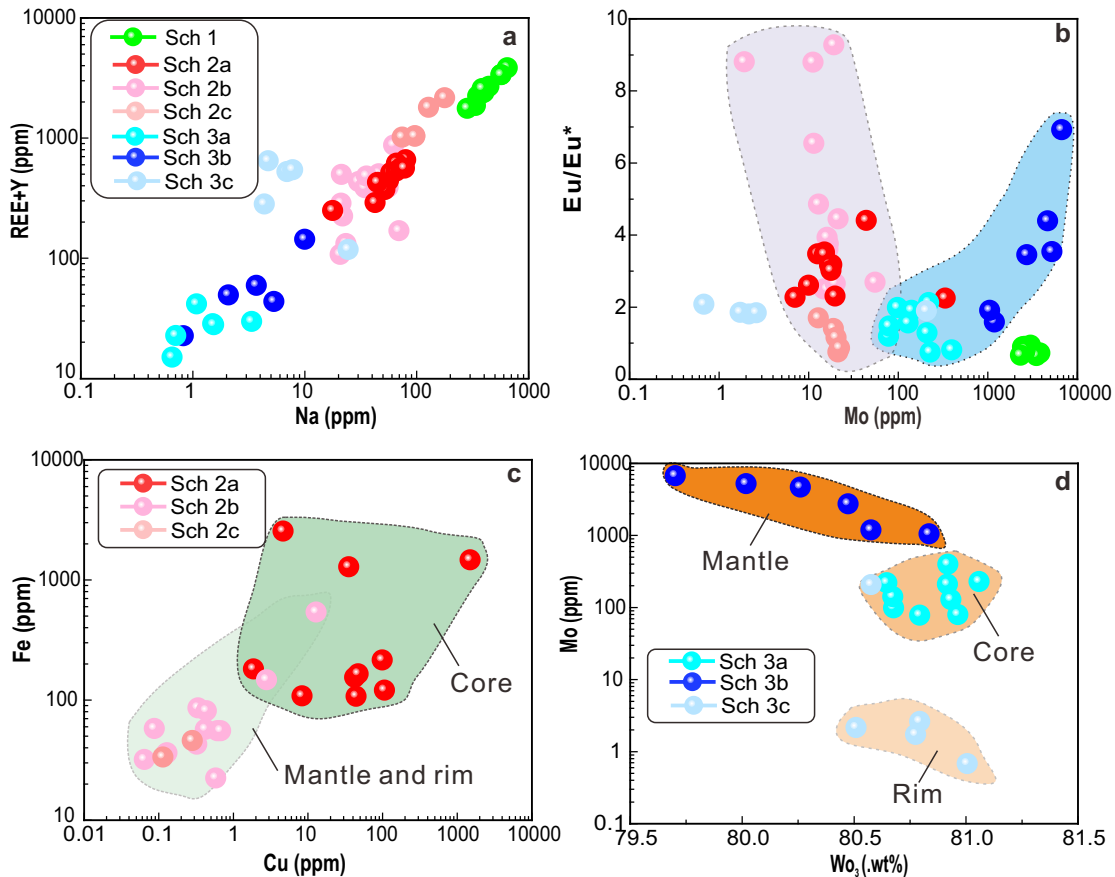


Figure 5

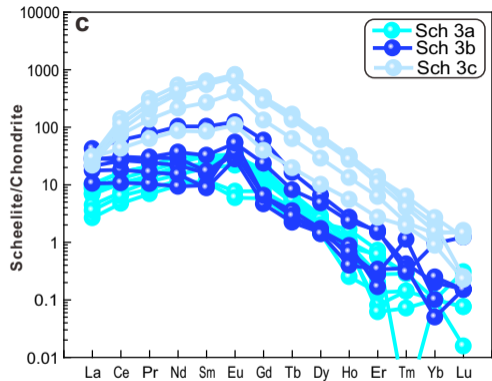
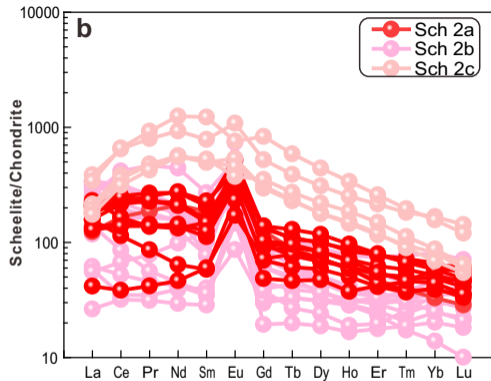
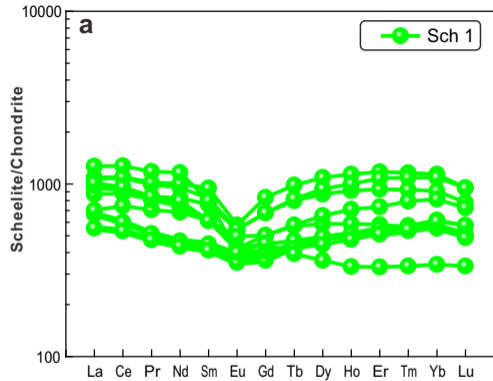


Figure 6

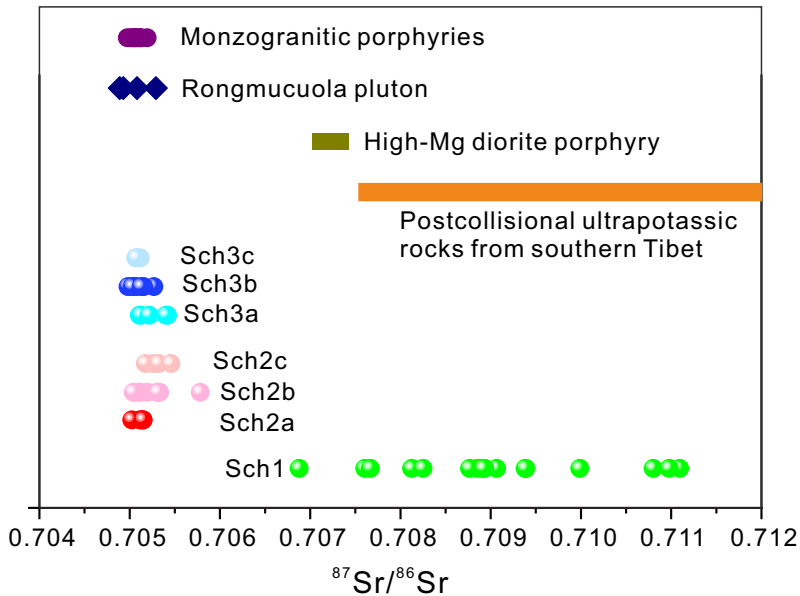


Figure 7

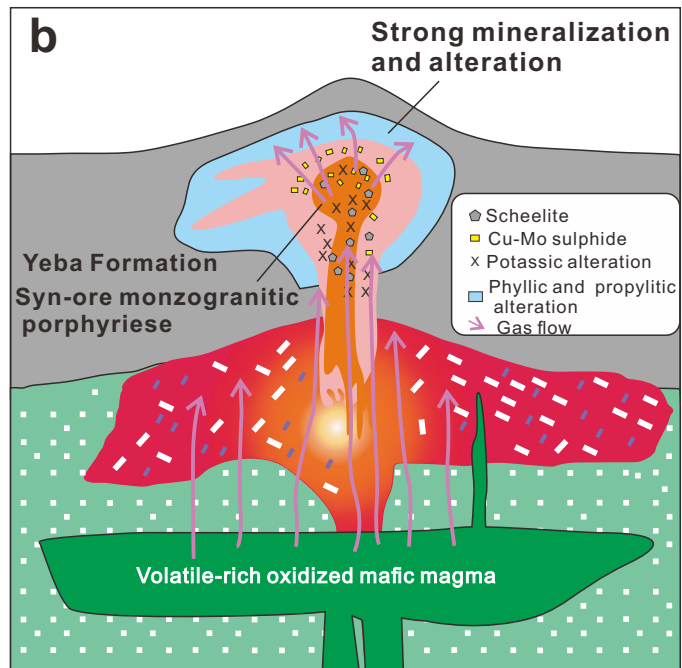
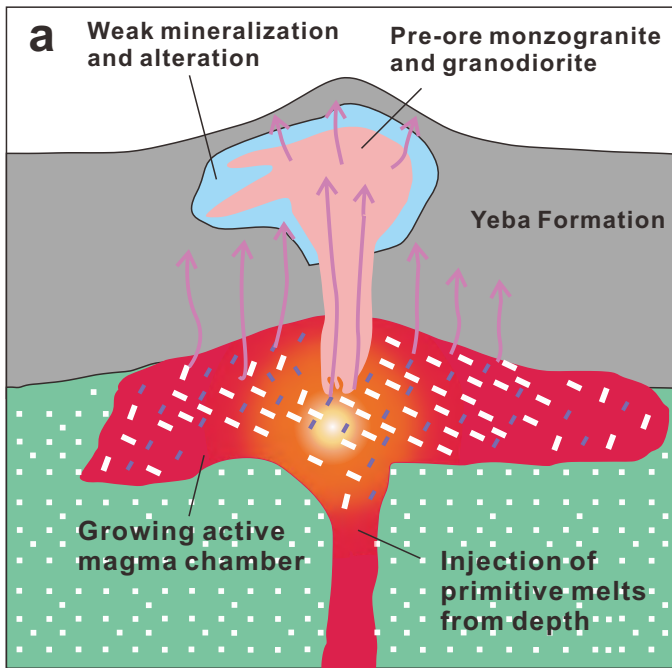


Figure 8